

Article

Borate Anion Dopant Inducing Oxygen Vacancies over Co_3O_4 Nanocages for Enhanced Oxygen Evolution

Xuetao Liu, Heng Liu, Guangling He, Yanlin Zhu, Jiamin Xiao and Lei Han *

Hunan Joint International Laboratory of Advanced Materials and Technology for Clean Energy, College of Materials Science and Engineering, Hunan University, Changsha 410082, China; liuxt2018@hnu.edu.cn (X.L.); liuheng419@hnu.edu.cn (H.L.); hegl@hnu.edu.cn (G.H.); yanlinzhu@hnu.edu.cn (Y.Z.); xjm0304@hnu.edu.cn (J.X.)
* Correspondence: hanlei@hnu.edu.cn

Abstract: The rational design of cost effective and highly efficient oxygen evolution reaction (OER) catalysts plays an extremely important role in promoting the commercial applications of electrochemical water splitting. Herein we reported a sacrificial template strategy for the preparation of borate anion doped Co_3O_4 @ZIF-67 nanocages assembled with nanosheets ($\text{B-Co}_3\text{O}_4$ @ZIF-67) by hydrothermal boronation of zeolitic imidazolate framework-67 (ZIF-67). During the preparation process, two different kinds of borate anion sources were found to regulate the morphological structures by tuning the etching rate between ZIF precursors and the borate anion. Moreover, borate anion doping was also found to induce oxygen vacancy defects, which is beneficial for modulating the electronic structure and accelerating electron transport. Meanwhile, the resultant $\text{B-Co}_3\text{O}_4$ @ZIF-67 nanocages possess a large specific surface area, which is beneficial for the mass transfer of the electrolyte and exposing more catalytic active sites. Benefiting from the advantages above, the resultant $\text{B-Co}_3\text{O}_4$ @ZIF-67 nanocages exhibit impressive OER performance with a small overpotential of 334 mV, a current density of 10 mA cm^{-2} , a small Tafel slope of $73.88 \text{ mV dec}^{-1}$, as well as long-term durability in an alkaline electrolyte.



Citation: Liu, X.; Liu, H.; He, G.; Zhu, Y.; Xiao, J.; Han, L. Borate Anion Dopant Inducing Oxygen Vacancies over Co_3O_4 Nanocages for Enhanced Oxygen Evolution. *Catalysts* **2021**, *11*, 659. <https://doi.org/10.3390/catal11060659>

Academic Editor: Thomas Wågberg

Received: 2 May 2021
Accepted: 19 May 2021
Published: 22 May 2021

Publisher's Note: MDPI stays neutral with regard to jurisdictional claims in published maps and institutional affiliations.



Copyright: © 2021 by the authors. Licensee MDPI, Basel, Switzerland. This article is an open access article distributed under the terms and conditions of the Creative Commons Attribution (CC BY) license (<https://creativecommons.org/licenses/by/4.0/>).

Keywords: Co_3O_4 nanocages; borate anion dopant; oxygen vacancies; oxygen evolution

1. Introduction

Hydrogen as a clean energy carrier with high energy density ($282 \text{ kJ} \cdot \text{mol}^{-1}$) is considered most promising for replacing traditional fossil fuels to cope with the increasing global energy demand and environmental issues [1–4]. Electrochemical water splitting ($2\text{H}_2\text{O} \rightarrow 2\text{H}_2 + \text{O}_2$), consisting of two half reactions of the oxygen evolution reaction (OER) and the hydrogen evolution reaction (HER), provides a green technology for hydrogen production through the use of renewable energy (such as wind energy, solar energy, tidal energy, etc.) [5–7]. Relative to the HER, the OER is a four-electron proton coupled transfer process, and possesses sluggish kinetics, severely limiting the efficiency of overall water splitting [8–10]. To date, the state-of-the-art OER catalysts mainly focus on precious metal catalysts (such as RuO_2 and IrO_2), but their scarcity and high cost limit their implementation in practical commercial applications [11,12]. Therefore, it is essential, yet remains a huge challenge for development of cost effective and highly efficient oxygen evolution reaction (OER) catalysts.

Recently, various transition-metal-based materials, including transition metal oxides [13], phosphides [14,15], sulfides [16], borides [17], (oxy) hydroxides [18], and layered double hydroxides (LDHs) [19,20], have been widely studied as a promising substitute to precious metal OER catalysts. Particularly, Co_3O_4 -based materials have received increasing attention as promising alternatives due to their good OER catalytic activity in alkaline solution [21,22]. Nevertheless, the poor electronic conductivity of Co_3O_4 is the main bottleneck hindering the improvement of its OER activity [23,24]. In this regard, the regulation in morphological and electronic structure has been reported as an effective way to improve

the electrochemical performances of Co_3O_4 -based materials [25–27]. On one hand, the unique nanostructures, such as nanosheets and nanocages, usually possess large specific surface area, which are beneficial to the mass transport and exposure of catalytically active sites, and the release of the generated gas during the water splitting process [24,27–30]. On the other hand, recent studies have shown that the introduction of dopants can induce the formation of a large number of oxygen vacancy defects, increasing electronic conductivity and promoting the improvement of electrochemical OER performance [31,32]. For instance, the introduction of boron into transition metal compounds was reported to induce vacancy defects and result in the generation of large numbers of catalytically active sites, promoting the improvement of electrochemical performances [24,31,33]. Based on the above considerations, it can be reasonable to conclude that high OER catalytic activity can be expected for heteroatom-doped Co_3O_4 -based materials with nanocage structures composed of ultrathin nanosheets.

Metal–organic frameworks (MOFs), consisting of inorganic metal ions/clusters coordinated with organic ligands, are distinctive organic–inorganic hybrid porous materials with controllable porous structures, high specific surface areas and well-tunable structures [34,35]. Because of these unique structural merits, MOFs and their derivatives have been widely applied in energy storage and conversion [36,37], gas adsorption and separation [38,39] and other research fields. Generally, MOFs are used as sacrificial templates for the fabrication of various nanostructured materials that inherit the advantages of their precursors [8]. The large specific surface area of MOFs-derived nanostructured materials is conducive to exposing more catalytically active sites and promoting charge and mass transfer during the OER process [40]. Inspired by this, herein we propose an easy and effective strategy for the synthesis of MOF-derived borate anion doped cobalt oxide ($\text{B-Co}_3\text{O}_4@\text{ZIF-67}$) nanocages assembled with nanosheets by hydrothermal boronation. Meanwhile, the type of boron source and solvent system were also optimized, and borate-buffered methanol was found to be the optimal condition for the formation of unique nanocage structures composed of nanosheets. The unique nanocage structures create the large specific surface area ($705.77 \text{ m}^2\text{g}^{-1}$), thus facilitating the exposure of catalytically active sites and accelerating mass transfer and gas release during the OER process. Moreover, borate anion doping is also conducive to the formation of oxygen vacancy defects, thus modulating the electronic structure of atoms and promoting improvement in catalytic OER activity. As expected, the resultant $\text{B-Co}_3\text{O}_4@\text{ZIF-67}$ exhibited superior OER activity in alkaline solution.

2. Results and Discussion

The schematic illustration for the preparation of the $\text{B-Co}_3\text{O}_4\text{-2}@\text{ZIF-67}$ nanocages is shown in Figure 1. Briefly, the uniform ZIF-67 nanocubes were first synthesized by the reaction of $\text{Co}(\text{NO}_3)_2 \cdot 6\text{H}_2\text{O}$ with 2-methylimidazole under the assistance of CTAB. Subsequently, $\text{B-Co}_3\text{O}_4\text{-2}@\text{ZIF-67}$ nanocages were successfully obtained through the hydrothermal reaction of ZIF-67 with borate buffers solution (BBS). The pH value of the BBS solution, containing a large amount of borate ion ($\text{B}_4\text{O}_7^{2-}$), was measured to be 9.5. During the hydrothermal reaction process, hydroxyl ions (OH^-) were produced through the hydrolysis of $\text{B}_4\text{O}_7^{2-}$, which then replaced 2-methylimidazole within ZIF-67 precursor to form $\text{Co}(\text{OH})_2$, which were finally transformed into B-doped Co_3O_4 under high temperatures due to the existence of dissolved oxygen and a lot of borate ions ($\text{B}_4\text{O}_7^{2-}$) in the reaction system [41].

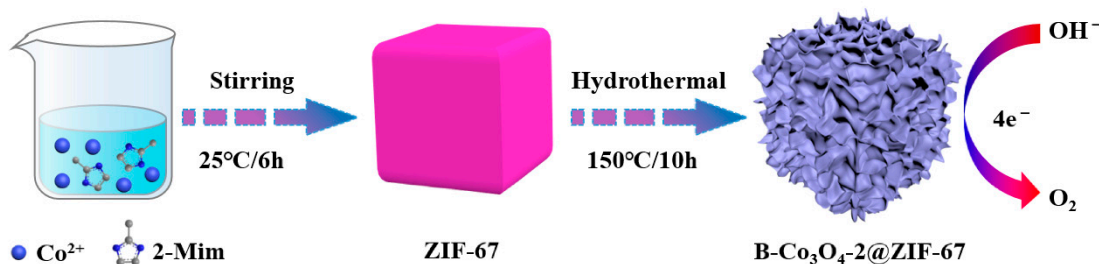


Figure 1. Schematic illustration of the preparation of B-Co₃O₄-2@ZIF-67 nanocages.

The morphological structures of the resultant ZIF-67 precursors and their derivatives were investigated by FESEM and TEM. As shown, uniform cubic morphology was observed for the resultant ZIF-67 precursor with an average size of 1 μm (Figures S1 and S2), which is in accordance with the previously reported results [42,43]. After the hydrothermal reaction of ZIF-67 precursor with BBS in methanol, the resultant ZIF-67 nanocubes were transformed into B-Co₃O₄-2@ZIF-67 nanocubes assembled with nanosheets (Figure 2a,b). TEM results demonstrated that the resultant B-Co₃O₄-2@ZIF-67 possesses hollow nanocages assembled from nanosheets with wrinkled edges (Figure 2c–e). Furthermore, there are no obvious lattice fringes from high-resolution HRTEM images and selective area electron diffraction (SAED) displays of the diffused rings (Figure 2f), both of which indicate the amorphous nature of the resultant B-Co₃O₄-2@ZIF-67 nanocages. Meanwhile, the EDX elemental mapping (Figure 2g) and the EDX spectra (Figure S3) reveal the uniform distributions of C, N, O, B, and Co in the resultant B-Co₃O₄-2@ZIF-67 nanocages. Interestingly, when we only used K₂B₄O₇·4H₂O as a boron source, nanosheets-assembled core-shell structured B-Co₃O₄-1@ZIF-67 can be obtained (Figure S4a,b), which could be further confirmed by TEM images (Figure S4c–e). Similarly, HRTEM images and SAED patterns also proved the amorphous nature of the resultant B-Co₃O₄-1@ZIF-67 (Figure S4f,g). In the contrast, CoBi/ZIF-67 is composed of the residual ZIF-67 and cobalt borate (Co–Bi) nanosheets in the presence of H₃BO₃ as a boron source (Figure S4h,i). We inferred that the formation of core–shell structure may be attributed to the incomplete etching process due to the insufficient amount of B₄O₇²⁻ only in the presence of K₂B₄O₇. Differently, boric acid used as a boron source can produce protons (H⁺) for the protonation of 2-methylimidazole, resulting in the release of Co²⁺ and then reacting with the borate ions (B₄O₇²⁻) to form cobalt borate (Co–Bi) nanosheets. In addition, the effect of the solvent in the reaction system on the morphology of the resultant catalysts was also investigated. Under the same reaction conditions, the introduction of water resulted in the complete destruction of morphology from the nanocubes into irregular structures (nanowires and nanoparticles) (Figure S5), which may be attributed to the fast etching rate. These results demonstrate that the morphologic structures of the resultant catalysts can be regulated through tuning the boron source and solvent during the preparation process. Besides, potassium hydroxide was selected as a substitute of K₂B₄O₇·4H₂O to provide an alkaline environment. Only a small number of nanosheets were formed on the surface of ZIF-67 precursor, but the cubic morphology of ZIF-67 precursor was still well-retained (Figure S6). These results demonstrate that the presence of borate ion is essential for the formation of nanocages.

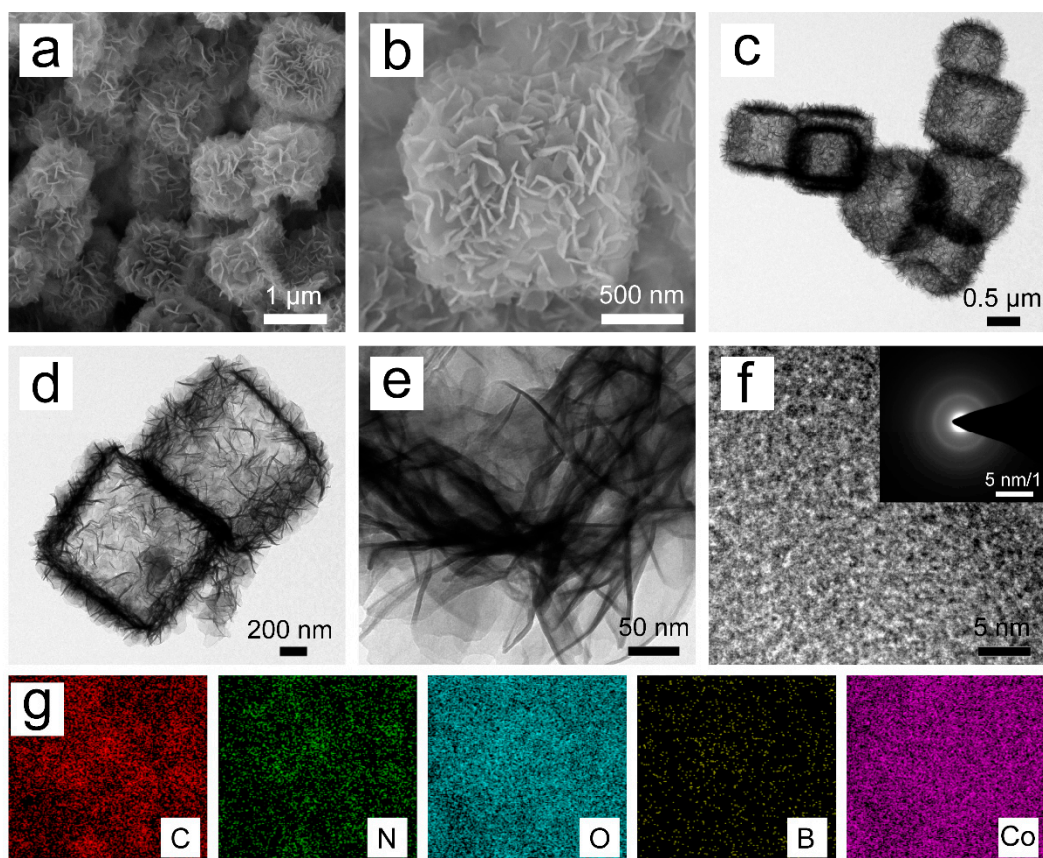


Figure 2. (a,b) FESEM images, (c–e) TEM images (f) HRTEM image (the inset showing the SAED pattern), and (g) Element mappings of C, N, O, Co, B and P images of the resultant B-Co₃O₄-2@ZIF-67 electrocatalyst.

The phase composition and crystal structure of the resultant materials were characterized by XRD. As observed, there are residual ZIF-67 precursors in the resultant B-Co₃O₄-2@ZIF-67, B-Co₃O₄-1@ZIF-67, and CoBi/ZIF-67 regardless of the type of boron source (Figure S7), which could be clearly observed from TEM images (Figure S4). Nevertheless, the diffraction peak intensity assigned to ZIF-67 obviously decreases for the resultant B-Co₃O₄-2@ZIF-67, implying the more thorough etching of ZIF-67 precursor when reacting with the BBS solution compared to K₂B₄O₇ and H₃BO₃. Besides, there are not any crystal diffraction peaks except for those assigned to ZIF-67, demonstrating the amorphous nature of the newly formed nanosheets after reacting with different boron sources. Unexpectedly, all of the diffraction peaks assigned to ZIF-67 disappeared completely whereas new diffraction peaks indexed to the Co₃O₄ (JCPDS No. 74-2120) could be observed after the introduction of water in the reaction system (Figure S8a) [44]. Moreover, the diffraction peak intensity increased as the addition of water increased, which may explain why there is poor crystallinity for the resultant B-Co₃O₄-2@ZIF-67 nanocages despite the introduction of a very small amount of water from K₂B₄O₇·4H₂O. It should be noted that no peaks assigned to cobalt borate were detected for all of the above XRD patterns, indicating that there was no formation of a new crystalline phase after the addition of a boron source. Careful observation demonstrates the appearance of the diffraction peak assigned to the (511) crystal plane of Co₃O₄ in the XRD patterns of the resultant B-Co₃O₄-1, B-Co₃O₄-2 and B-Co₃O₄-2@ZIF-67 (Figure S8b), which all shifted the lower Bragg angle relative to standard diffraction peak (59.35°) of the (511) crystal plane of Co₃O₄. The negative shift of the Bragg angle indicates the expansion of the crystal lattice at the same incident wavelength [45], indicating that boron as dopant may be incorporated into the crystal structure Co₃O₄. Based on the XRD results, we inferred that B-doped cobalt oxide (denoted as B-Co₃O₄) was successfully formed by replacing oxygen ions (140 pm) in cobalt oxide with borate ions

(191 pm) [2]. In order to further confirm the successful synthesis of B-Co₃O₄, the resultant B-Co₃O₄-2@ZIF-67 samples were further annealed at 700 °C for 1 h in air atmosphere. As shown in Figure S8c, eight diffraction peaks at 19.0°, 31.3°, 36.8°, 38.5°, 44.8°, 56.6°, 59.3°, and 65.2° can be assigned to the Co₃O₄ (JCPDS No. 74-2120). Meanwhile, it is worth noting that four diffraction peaks at 19.8, 30.0°, 31.6° and 34.2° were also detected, which can be indexed to the Co₂B₂O₅ (JCPDS No. 98-09-6562) phase. Besides, the EDX element mapping and the EDX spectra also verify the presence of B elements in the resultant B-Co₃O₄-1 and B-Co₃O₄-2 (Figure S9 and Table S2), further confirming the successful doping of B into the Co₃O₄.

FT-IR spectra were also performed to investigate the surface functional groups and the skeleton changes of the resultant catalysts [46]. For ZIF-67 precursor, there is the apparent stretching vibration at 425 cm⁻¹ related to the characteristic peak of Co–N (Figure S10), which confirms the bonding between the cobalt atom and the N atom in the 2-methylimidazole linker in ZIF-67 [47]. The peaks in the region of 600–1500 cm⁻¹ contribute to the bending and stretching modes of the imidazole ring in ZIF-67 [48]. The characteristic peaks at 693 cm⁻¹ and 756 cm⁻¹ can be ascribed to the out-of-plane bending vibration mode of the imidazole ring [49], while the in-plane bending vibration of the imidazole ring can be observed at 900–1350 cm⁻¹ [50]. Additionally, the obvious characteristic peaks in the range 1350–1500 cm⁻¹ can be attributed to the stretching vibration mode of the ring [51]. The peak at 1580 cm⁻¹ can be associated with the stretching vibration of the C=N bond in 2-methylimidazole ligand [52]. Moreover, the peak at 2929 cm⁻¹ and 3134 cm⁻¹ are caused by the C-H stretching vibration of the aromatic ring and the aliphatic methyl group in 2-methylimidazole, respectively [47]. The above results demonstrate the successful synthesis of the ZIF-67 precursor. After the reaction of ZIF-67 precursor with different boron sources, there is new peak vibration in the range 480–660 cm⁻¹ corresponding to the formation of a metal–oxygen bond (M–O) [53]. Meanwhile, the intensity of the vibration peak assigned to the ZIF-67 precursor decreases with the amount of boron source added, indicating the transformation of ZIF-67 into other components. Some characteristic peaks related to ZIF-67 precursor almost disappear after the introduction of water (Figure S11), indicating that the material skeleton on the surface of ZIF-67 collapsed [46]. Meanwhile, there are two sharp characteristic peaks at 575 cm⁻¹ and 667 cm⁻¹ in the spectra, which contributed to the stretching vibration mode of octahedral coordinated Co³⁺–O bonding and tetrahedral coordinated Co²⁺–O bonding in Co₃O₄, respectively [54,55]. The broad absorption peak at 3440 cm⁻¹ is due to the vibration of O–H from surface water molecules [51,56]. These results demonstrate that the main component was Co₃O₄ after the introduction of water, which is consistent with the XRD results. Combined with the appearance of metal–oxygen bonds after the introduction of different boron sources, we can infer that we successfully synthesized B-Co₃O₄.

In addition, UV-Vis absorption spectra were also carried out by dispersing the resultant catalysts into ethanol with a constant concentration in the range of 400 to 700 nm. As displayed in Figure S12, the ZIF-67 precursor has characteristic transitions of tetrahedral Co²⁺ at 539 nm and 596 nm, respectively [47]. Moreover, the characteristic transition peak can be well-retained after reaction with different boron sources and potassium hydroxide, and the intensity of the B-Co₃O₄-2@ZIF-67 peak is much lower than that of the ZIF-67 precursor, indicating that there remain ZIF-67 residues in the resultant B-Co₃O₄-2@ZIF-67, which is consistent with the above mentioned FESEM and TEM analysis results.

Nitrogen adsorption–desorption isotherms were performed to investigate the specific surface area of the resultant B-Co₃O₄-1@ZIF-67 and B-Co₃O₄-2@ZIF-67 [57]. The specific surface area of the resultant B-Co₃O₄-2@ZIF-67 as calculated to be 705.77 m²g⁻¹, which is higher than that of the resultant B-Co₃O₄-1@ZIF-67 (398.29 m²g⁻¹) (Figure S3a). In addition, a hysteresis loop with type-IV isotherm could be observed in the resultant B-Co₃O₄-2@ZIF-67 and B-Co₃O₄-1@ZIF-67, indicating the existence of mesoporous structures [58]. The pore size distribution results demonstrate (Figure 3b that the resultant B-Co₃O₄-2@ZIF-67 mainly contained micropores whereas the resultant B-Co₃O₄-1@ZIF-67 was dominated by

mesopores, with their average pore diameters being 2.97 and 7.98 nm, respectively [59]. The large specific surface area and microporous structure of the resultant B-Co₃O₄-2@ZIF-67 are beneficial for exposing more active sites and accelerating mass transfer, which can improve the catalytic activity of OER [60].

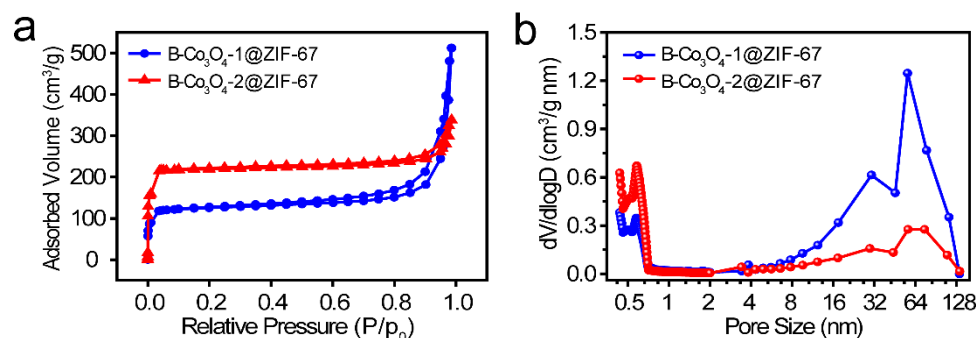


Figure 3. (a) N₂ adsorption-desorption isotherms and (b) the corresponding pore size distribution of the resultant B-Co₃O₄-1@ZIF-67 and B-Co₃O₄-2@ZIF-67.

The surface chemical composition and element valence states of the resultant catalysts were further evaluated by XPS. The XPS survey spectra (Figure 4a and Figure S12a) revealed the existence of C, N, O, B, and Co elements on the surface of the resultant B-Co₃O₄-1@ZIF-67 and B-Co₃O₄-2@ZIF-67, which is consistent with the EDX element mapping results (Figure 2g), while the resultant Co(OH)₂@ZIF-67 contains C, N, O, and Co elements. In the high-resolution Co XPS 2p spectra of Co(OH)₂@ZIF-67 samples (Figure S12b), there are two strong peaks at binding energies of 781.57 eV and 797.16 eV corresponding to Co²⁺ species whereas the other two peaks at 780.10 eV and 795.80 eV can be attributed to Co³⁺ species [8,56,61]. In addition, the other two peaks at 785.06 eV and 801.71 eV are shakeup satellite peaks. Specifically, by calculating the integrated peak area, the atomic ratio of Co³⁺/Co²⁺ is 1.13 in the resultant Co(OH)₂@ZIF-67, implying the partial oxidation of Co²⁺ in alkaline solution during the hydrothermal process. Compared with Co(OH)₂@ZIF-67, the binding energy of Co²⁺ (781.89 eV) and Co³⁺ (780.48 eV) has a significant positive shift in the resultant B-Co₃O₄-1@ZIF-67, demonstrating that doping with electron negativity borate anions induced the formation of a higher oxidation state [33]. This phenomenon may be attributed to the electron transfer from Co atoms to the borate anion dopant due to the large electron negativity of the borate anion relative to that of the metal Co [62]. In addition, the integrated peak area ratio of Co³⁺/Co²⁺ was calculated to be 0.961 in the resultant B-Co₃O₄-1@ZIF-67, which is lower than the theoretical value of Co³⁺/Co²⁺ (2:1) in Co₃O₄. It should be here noted that a certain amount of Co²⁺ in the resultant B-Co₃O₄-1@ZIF-67 comes from the coordinated Co atoms of the ZIF-67 residues. Similarly, the more positive shift in binding energy of Co²⁺ (782.20 eV) and Co³⁺ (780.80 eV) in the resultant B-Co₃O₄-2@ZIF-67 was observed compared to the resultant B-Co₃O₄-1@ZIF-67 (Figure 4b), and the intensity of Co³⁺/Co²⁺ was 1.15. The obvious change in binding energy may be attributed to the introduction of more borate anions when reacting the ZIF-67 precursor with the BBS solution (Table S3), which can be further confirmed by the high-resolution B 1s XPS spectra of B-Co₃O₄-2@ZIF-67 (Figure 4c). As shown, the peak at 192.3 eV, which is assigned to three-coordinated borate species (B–O), proved that boron atoms in the form of borate were incorporated into the crystal structure of Co₃O₄ [63,64]. In this process, B₄O₇²⁻ partially replaced the oxygen anions (O²⁻) in the Co₃O₄ lattice, thereby destroying the original crystalline structure and producing a large number of oxygen vacancy defects [27,65]. Therefore, we used electron paramagnetic resonance (EPR) spectra to analyze and detect the content of unpaired electronic species (oxygen vacancy defects) in the resultant B-Co₃O₄-1@ZIF-67 and B-Co₃O₄-2@ZIF-67 [27]. As shown in Figure S14, the resultant B-Co₃O₄-2@ZIF-67 produces more high-energy dangling bonds than B-Co₃O₄-1@ZIF-67, indicating that the resultant B-Co₃O₄-2@ZIF-67 possesses higher

concentrations of oxygen vacancy defects [32]. It has been reported that the introduction of defects is beneficial for exposing more catalytically active sites.

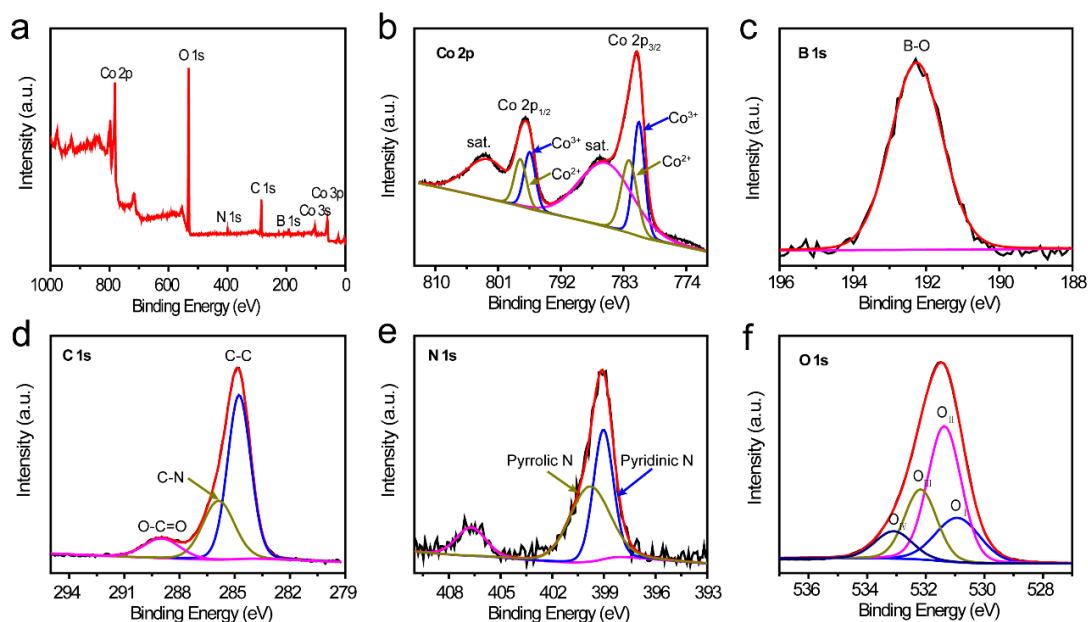


Figure 4. (a) The XPS survey spectra, (b) high-resolution Co 2p spectra, (c) high-resolution B 1s spectra, (d) C 1s spectra, (e) N 1s spectra, and (f) O 1s spectra of the resultant B-Co₃O₄-2@ZIF-67.

In the high-resolution C 1s spectra of B-Co₃O₄-2@ZIF-67 (Figure 4d), there are three distinct characteristic peaks at 284.8, 285.9, and 289.0 eV, which are attributed to sp² bonded carbon (C–C), sp² hybrid C–N bonds, and the bond between carbon and surface oxygen (O–C=O), respectively [66,67]. The high-resolution N 1s XPS spectra (Figure 4e) can be deconvoluted into three peaks corresponding to the pyridine-N (399.0 eV) and pyrrolic-N (399.8 eV) [68]. As shown in Figure 4f, the high-resolution O 1s XPS spectra can be divided into four characteristic peaks, where the binding energy at 530.9 contributes to the lattice oxygen (M–O, O_I), and the binding energy at 531.36 eV can be assigned to the oxygen vacancy (V_O, O_{II}) [31]. The resultant B-Co₃O₄-1@ZIF-67 and B-Co₃O₄-2@ZIF-67 both have vacant oxygen (V_O, O_{II}) peaks whereas Co(OH)₂@ZIF-67 only contains two oxygen species of lattice oxygen (M–O, 530.74 eV) and adsorbed oxygen (O_{III}, 531.53 eV) (Figure S12f), proving that the introduction of boron leads to the formation of oxygen vacancy defects. The existence of oxygen vacancy defects has been reported to facilitate the adsorption of water molecules and OH[−] anions during the OER process, thus promoting the water oxidation process [69]. Additionally, the binding energy at 532.2 and 533.1 eV were associated with the adsorbed oxygen species (O_{III}) and surface water molecules (O_{IV}) on the catalysts' surface, respectively [70].

The electrocatalytic OER performances of the resultant catalysts were investigated in a typical three-electrode system with a rotating disk electrode (RDE) at the rotating speed of 1600 rpm in 1.0 MKOH. The catalyst loading amount was fixed at 0.5 mg/cm², and all electrochemical data has been corrected by iR_s compensation to eliminate the influence of ohmic voltage drop [71]. As shown in Figure 5a and Table S4, the resultant B-Co₃O₄-2@ZIF-67 exhibits the best OER performance with the largest current density among the investigated catalysts. Moreover, the overpotential at a current density of 10 mA cm^{−2} is 334 mV for the resultant B-Co₃O₄-2@ZIF-67, which is significantly lower than that of B-Co₃O₄-1@ZIF-67 (349 mV) and CoBi/ZIF-67 (341 mV). Besides, the lower OER performances of the resultant B-Co₃O₄-1 (351 mV) and B-Co₃O₄-2 (346 mV) prepared by the introduction of water were observed compared to the B-Co₃O₄-2@ZIF-67 (Figure S15a and Table S4). In addition, the OER performance of the resultant B-Co₃O₄-2@ZIF-67 was also superior to that of the resultant Co(OH)₂@ZIF-67 (343 mV) and ZIF-67 precursor (371

mV) (Figure S16a and Table S4). The catalytic kinetics parameter is generally used to evaluate the catalytic performances of the resultant catalysts. In order to get insight into the OER kinetics, a Tafel plot was obtained from the polarization curve according to the Tafel equation [59]: $\eta = b \log j + \alpha$, where η is the overpotential, j is the current density, b is the Tafel slope, and α is the constant. The resultant B-Co₃O₄-2@ZIF-67 presents a smaller Tafel slope (73.88 mVdec⁻¹) than the resultant B-Co₃O₄-1@ZIF-67 (122.8 mVdec⁻¹) and B-Co₃O₄/ZIF-67 (99.28 mV dec⁻¹) (Figure 5b and Table S4), indicating more favorable OER catalytic kinetics for the resultant B-Co₃O₄-2@ZIF-67. The information of the rate determination step during the OER process can be acquired from the Tafel slope [2,72]. When the Tafel slope is less than 40 mVdec⁻¹ and greater than 120 mVdec⁻¹, the formation of *OOH ($O^* + OH^- \rightarrow *OOH + e^-$, where * represents the catalytic active site on the catalysts surface) and *OH ($* + OH^- \rightarrow *OH + e^-$) are the rate-determining steps, whereas the Tafel slope located between the above two values, the formation of O* ($*OH + OH^- \rightarrow *O + H_2O + e^-$) is the rate-determining step. Therefore, the formation of O* is the rate-determining step during the OER process over the resultant B-Co₃O₄-2@ZIF-67.

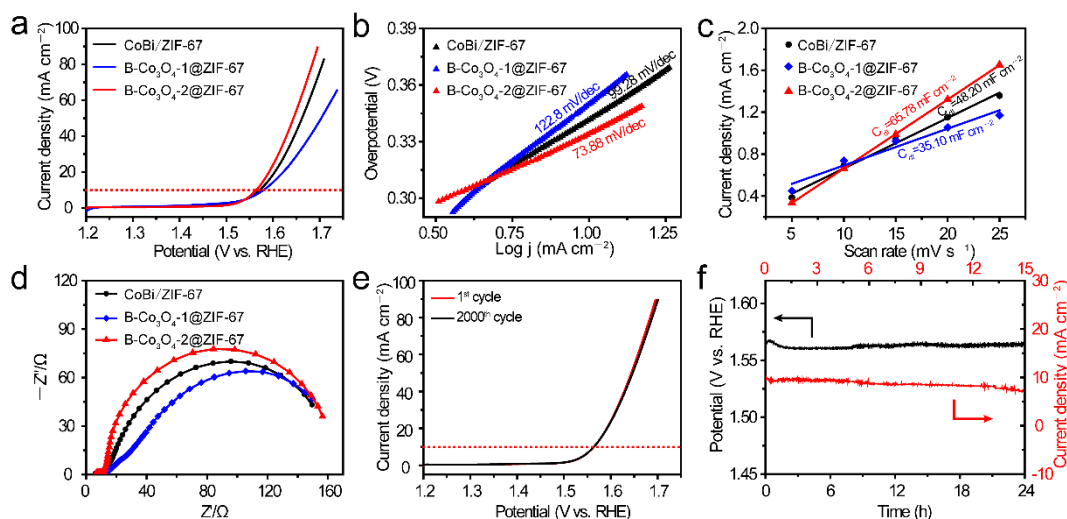


Figure 5. Electrochemical performances of the resultant CoBi/ZIF-67, B-Co₃O₄-1@ZIF-67, and B-Co₃O₄-2@ZIF-67 in 1.0 M KOH: (a) polarization curves with iR_s compensation, (b) Tafel slope plots, (c) current density as a function of scan rate derived from the CV curves at different scan rates, (d) Nyquist plots, (e) polarization curves of the resultant B-Co₃O₄-2@ZIF-67 before and after 2000 CV cycles, and (f) chronopotentiometry at the fixed current density of 10 mA cm⁻² and the chronoamperometry at the fixed potential corresponding to the current density of 10 mA cm⁻² of the resultant B-Co₃O₄-2@ZIF-67.

It is well known that a highly electrochemically active surface area (ECSA) is beneficial for improving catalytic activity. Cyclic voltammetry (CV) was carried out at different scan rates in the non-faradaic potential region from 1.2 to 1.3 V vs. RHE due to the proportional relationship between ECSA and electrochemical double-layer capacitance (C_{dl}) [73]. As expected, the resultant B-Co₃O₄-2@ZIF-67 exhibited the high C_{dl} value of 65.78 mFcm⁻², which is much higher than that of the resultant B-Co₃O₄-1@ZIF-67 (35.10 mFcm⁻²) and CoBi/ZIF-67 (48.20 mFcm⁻²), and the other resultant catalysts (Figure 5c, Figures S17 and S18; Table S4). The large ECSA of the resultant B-Co₃O₄-2@ZIF-67 may be due to its unique nanosheets-assembled nanocage structure, thus exposing more catalytic active sites during the OER process [74]. Electrochemical impedance spectroscopy (EIS) measurements were also performed to explore the interfacial charge transport properties of these catalyst modified electrodes [75]. Unexpectedly, the resultant B-Co₃O₄-2@ZIF-67 exhibited a larger charge transfer resistance (R_{ct}) than the resultant CoBi/ZIF-67, B-Co₃O₄-1@ZIF-67 (Figure 5d). In addition, the resultant B-Co₃O₄-1 and B-Co₃O₄-2 also exhibited a similar R_{ct} with the resultant B-Co₃O₄-2@ZIF-67 (Figure S15d). However, the

R_{ct} of the resultant B-Co₃O₄-2@ZIF-67 was smaller than that of the resultant ZIF-67 precursor and Co(OH)₂@ZIF-67 (Figure S16c). These results show that the R_{ct} of the resultant ZIF-67 can be significantly reduced by one-step hydrothermal boronation treatment, but it is not the dominant factor affecting the catalytic performance of the resultant catalysts.

Long-term stability is another important parameter for evaluating the practical applications of the resultant catalyst [11]. In this regard, continuous CV cycles were conducted over the resultant B-Co₃O₄-2@ZIF-67 in the potential range from 1.2 to 1.5 V at the scan rate of 100 mVs⁻¹ in 1.0 M KOH. No obvious decay in the current density was observed after 2000 CV cycles over the resultant B-Co₃O₄-2@ZIF-67 (Figure 5e). Meanwhile, the durability was also evaluated by chronopotentiometry at a current density of 10 mAcm⁻² for 24 h, and chronoamperometry at the constant of potential corresponding to a current density of 10 mAcm⁻² for 15 h. No obvious changes in potential and current density were observed after continuous operation (Figure 5f). These results suggest the excellent long-term durability of the resultant B-Co₃O₄-2@ZIF-67 in alkaline media. We also found that the morphologic structure of the resultant B-Co₃O₄-2@ZIF-67 can be well-retained after a long-term OER durability test (Figure S19). The composition and chemical state of the resultant B-Co₃O₄-2@ZIF-67 was further investigated by XPS after the long-term OER durability test (Figure S20). High-resolution Co 2p XPS spectra revealed that the intensity of the Co³⁺ (795.22 eV) peak is significantly higher than that of Co²⁺ (780.12 eV), and the ratio of Co³⁺/Co²⁺ increased from 1.15 to 1.22, indicating that the low-valence Co²⁺ is irreversibly oxidized to the high-valence Co³⁺ during the OER process (Figure S20a and Table S3). Differently, B 1s signal peak completely disappeared after the OER (Figure S20b), which may be due to the fact that the B element on the catalyst surface dissolved into the electrolyte during the OER process under the high potential [31]. As shown in Figure S20d, the peaks of the metal-oxygen bond (M–O, 929.10 eV, vacant oxygen (Vo, 531.15 eV), and adsorbed oxygen (532.49 and 535.45 eV) are clearly observed after the OER. The above results demonstrate that the oxygen vacancies caused by borate doping play an important role in the improvement of OER catalytic activity.

3. Experimental Section

3.1. Materials

Cobalt nitrate hexahydrate (Co (NO₃)₂·6H₂O, AR), 2-methylimidazole (C₅H₈N₂, AR), hexadecyl trimethyl ammonium bromide (CTAB, 99%), potassium tetraborate tetrahydrate (K₂B₄O₇·4H₂O, AR), boric acid (H₃BO₃, AR), methanol (AR), and potassium hydroxide (KOH, AR) were purchased from Sinopharm Chemical Reagent Co., Ltd (Shanghai, China). All chemicals were used without further purification.

3.2. Materials Synthesis

ZIF-67 cubes were firstly prepared according to the previously reported method with slight modification [42]. 0.87 g of Co(NO₃)₂·6H₂O was dissolved in 30 mL of 0.5 mg mL⁻¹ CTAB solution under the assistance of bath ultrasonication (550 W, 40 KHz, KunShan Ultrasonic Instruments, KQ 3200E, Kunshan, China) at room temperature to form solution A, and 13.62 g of 2-methylimidazole was dissolved in 30 mL of deionized water under magnetic stirring to form solution B. After that, the solution A was rapidly introduced into the solution B under vigorous stirring for 6 h at room temperature. The resultant purple precipitate was collected by centrifugation (2000 rpm for 8 min, Maikere, VL-65B, Changsha, China), washed by ethanol six times, and dried at 70°C overnight for further use.

B-Co₃O₄@ZIF-67 nanocages were synthesized by hydrothermal reaction. Typically, 1.5 mmol K₂B₄O₇·4H₂O and 4.5 mmol H₃BO₃ were dissolved in 30 mL of methanol under bath ultrasonication at room temperature for 40 min (550 W, 40 KHz), and 120 mg of the resultant ZIF-67 was quickly added into the above solution under vigorous magnetic stirring and then stirred for 20 min. Subsequently, the mixed solution was transferred into a 50 mL Teflon-lined stainless-steel autoclave (PAILAN, Shanghai, China), and was sealed

and maintained at 150 °C for 10 h in an electric oven. After being naturally cooled to room temperature, the product was collected via centrifugation (5000 rpm for 5 min), washed with ethanol three times, and finally dried for 30 h at −60 °C in a freeze dryer (SCIENTZ, SCIENCE-10N, Ningbo, China) for further use, which was denoted as B-Co₃O₄-2@ZIF-67 (2 represents the number of boron sources). As comparisons, CoBi/ZIF-67 and B-Co₃O₄-1@ZIF-67 were also prepared through the same method except for the use of different boron sources: H₃BO₃ and K₂B₄O₇·4H₂O, respectively. B-Co₃O₄ was also prepared using 30 mL of deionized water and the mixture of water and methanol (*v/v* = 1:1) instead of methanol, and the resultant products were denoted B-Co₃O₄-1 and B-Co₃O₄-2, respectively. Meanwhile, Co(OH)₂@ZIF-67 was also prepared replacing K₂B₄O₇·4H₂O with KOH.

3.3. Physicochemical Characterization

Powder X-ray diffraction (XRD) patterns were recorded on a Bruker D8 Advance X-ray diffractometer (Karlsruhe, Germany) with Cu-K α radiation (λ = 1.5406 Å; scan rate: 5°/min). The morphologic structures were characterized by field-emission scanning electron microscopy (FESEM) on a MIRA3 TESCAN scanning electron microscope operating at 15.0 kV with transmission electron microscopy (TEM, FEI Tecnai G2 F20, Hillsboro, OR, USA) and equipped with an OXFORD X-max 80T energy-dispersive X-ray (EDX) system. Chemical valence and element analysis were conducted by X-ray photoelectron spectroscopy (XPS) on a Thermo Scientific K-Alpha+ instrument (Waltham, MA, USA) operating at 12 kV. All spectra took the C1's peak at binding energy of 284.80 eV as the energy standard. Fourier transform infrared spectroscopy (FT-IR) spectra (4000–400 cm^{−1}) were measured using KBr as the reference sample on a Thermo Scientific Nicolet iS10 FTIR spectrophotometer (Waltham, MA, USA). UV–Vis absorption spectra were recorded on a UV–Vis spectrophotometer (YOKE INSTRUMENT T2600, Shanghai, China) with a certain concentration (0.5 mg/mL) of catalyst samples in ethanol solution. The specific surface area and pore volume were measured using an AUTOSORB IQ analyzer and analyzed via nitrogen adsorption–desorption isotherm. The pore-size distributions were calculated from the nitrogen desorption isotherms via the Horvaih-Kawazoe (HK) and Barrett-Joyner-Halenda (BJH) methods. The electron paramagnetic resonance (EPR) spectra were recorded on a Bruker EMXplus spectrometer (Karlsruhe, Germany) operated at X-band 9.5 GHz at room temperature.

3.4. Electrochemical Measurements

The electrochemical performances were investigated using a CHI 760E electrochemical workstation (CH Instruments, Inc., Shanghai, China) in a typical three-electrode system at room temperature. The catalyst-modified glassy carbon electrode (GCE, diameter: 5 mm) was used as a working electrode, and the GCE was polished with alumina slurry followed by cleaning in water and ethanol successively with ultrasonication prior to use. A carbon rod (Yueci Electronics, Shanghai) and an Ag/AgCl with saturated KCl solution electrode (Pine Research Instrumentation, Durham, NC, USA) were used as the counter electrode and reference electrode, respectively. The catalyst inks were prepared through dispersing 5 mg of the resultant catalyst into a mixture of 980 μ L ethanol and 20 μ L Nafion (5 wt.%, DuPont, Shenzhen, China) under ultrasonication for 40 min. Then 20 μ L of the obtained ink was dropped on the surface of the polished GCE and dried in ambient conditions to form a uniform thin catalyst layer (we calculated the amount of catalyst loading to be 0.50 mg cm^{−2}). For the durability test, the electrode was also fabricated using carbon paper (CP, 1 cm² in area, Comston Technology, Shenzhen, China). All the measured potentials were converted to the reversible hydrogen electrode (RHE) according the equation: $E_{\text{RHE}} = E_{\text{Ag/AgCl}} + 0.215 + 0.059 \text{ pH}$. The 1.0 M KOH aqueous solution was used as the electrolyte for OER performance measurements. The rotation speed of the rotating disk electrode (RDE) was fixed at 1600 rpm for all the measurements. Prior to the linear sweep voltammetry (LSV) test, the working electrode was activated by applying continuous cyclic voltammetry (CV) several times between 1.2 and 1.5 V in

1.0 M KOH with a scan rate of 100 mVs^{-1} until the stable CV curves were obtained. The LSV curves were measured by sweeping the potential from 1.2 to 1.8 V vs. RHE with a scan rate of 5 mVs^{-1} . The electrochemical impedance spectroscopy (EIS) measurements were carried out in a frequency range from 100 KHz to 0.01 Hz at 1.5 V by applying an alternating current (AC) voltage with 5 mV amplitude. The electrochemical double layer capacitance (C_{dl}) of different catalysts were measured using cyclic voltammetry in a non-faradaic region from 1.2 to 1.3 V vs. RHE with different scan rates of 5, 10, 15, 20, and 25 mVs^{-1} . The durability of the catalyst was evaluated according to the following methods: a polarization curve after 2000 CV cycles, chronopotentiometry at the fixed current density of 10 mAcm^{-2} , and chronoamperometry at the fixed potential corresponding to the current density of 10 mAcm^{-2} . All electrochemical potentials were corrected by iR_s compensation except for the chronopotential curve. The equivalent circuit of electrochemical impedance spectroscopy (EIS) was fitted by ZView software (Southern Pines, NC, USA).

4. Conclusions

In summary, $\text{B-Co}_3\text{O}_4@\text{ZIF-67}$ nanocages composed of nanosheets have been successfully prepared by hydrothermal boronation, and investigated as OER catalysts. The optimal $\text{B-Co}_3\text{O}_4@\text{ZIF-67}$ nanocages exhibited superior OER activity with a small overpotential of 330 mV at the current density of 10 mAcm^{-2} and excellent long-term durability in 1.0 M KOH. The excellent OER performance of $\text{B-Co}_3\text{O}_4@\text{ZIF-67}$ can be attributed to the two following qualities: (1) large specific surface area from unique its nanocages structure assembled with nanosheets, which is helpful in promoting mass transfer and exposing more catalytically active sites; (2) the formation of oxygen vacancy defects induced by borate anion doping, which is beneficial for modulating the electronic structure and improving the conductivity of the catalyst.

Supplementary Materials: The following are available online at <https://www.mdpi.com/article/10.3390/catal11060659/s1>, Figure S1: FESEM images of the resultant ZIF-67 precursor, Figure S2: XRD pattern of the resultant ZIF-67 precursor and the simulated ZIF-67, Figure S3: EDX spectra of the resultant $\text{B-Co}_3\text{O}_4\text{-2}@\text{ZIF-67}$, Figure S4: (a and b) FESEM images, (c–e) TEM images, (f) HRTEM image, and (g) SAED pattern of the resultant $\text{B-Co}_3\text{O}_4\text{-1}@\text{ZIF-67}$; (h and i) FESEM images of the resultant $\text{CoBi}/\text{ZIF-67}$, Figure S5: FESEM images of the resultant $\text{B-Co}_3\text{O}_4\text{-1}$ (a,b) and $\text{B-Co}_3\text{O}_4\text{-2}$ (c,d), Figure S6: FESEM images of the resultant $\text{Co(OH)}_2@\text{ZIF-67}$, Figure S7: XRD patterns of the resultant $\text{B-Co}_3\text{O}_4\text{-1}@\text{ZIF-67}$, $\text{B-Co}_3\text{O}_4\text{-2}@\text{ZIF-67}$, and $\text{B-Co}_3\text{O}_4/\text{ZIF-67}$, Figure S8: (a) XRD patterns of the resultant $\text{B-Co}_3\text{O}_4\text{-1}$, $\text{B-Co}_3\text{O}_4\text{-2}$ and $\text{B-Co}_3\text{O}_4\text{-2}@\text{ZIF-67}$; (b) the expanded XRD patterns of the area in figure a; (c) XRD patterns of the annealed $\text{B-Co}_3\text{O}_4\text{-2}@\text{ZIF-67}$; (d) XRD patterns of the resultant $\text{Co(OH)}_2@\text{ZIF-67}$, Figure S9: EDX element mapping of C, O, B, and Co images of the resultant $\text{B-Co}_3\text{O}_4\text{-1}$ (a) and $\text{B-Co}_3\text{O}_4\text{-2}$ (b), Figure S10: FT-IR spectra of the resultant ZIF-67 precursor, $\text{B-Co}_3\text{O}_4\text{-1}@\text{ZIF-67}$, $\text{B-Co}_3\text{O}_4\text{-2}@\text{ZIF-67}$, and $\text{Co-Bi}/\text{ZIF-67}$, Figure S11: FT-IR spectra of the resultant ZIF-67 precursor, $\text{B-Co}_3\text{O}_4\text{-1}$, and $\text{B-Co}_3\text{O}_4\text{-2}$, Figure S12: UV-Visible spectra of the as-prepared ZIF-67 precursor and its derivatives: $\text{B-Co}_3\text{O}_4\text{-1}$, $\text{B-Co}_3\text{O}_4\text{-2}$, $\text{CoBi}/\text{ZIF-67}$, $\text{Co(OH)}_2@\text{ZIF-67}$, $\text{B-Co}_3\text{O}_4\text{-1}@\text{ZIF-67}$ and $\text{B-Co}_3\text{O}_4\text{-2}@\text{ZIF-67}$, Figure S13: (a) The XPS survey spectra, (b) high-resolution Co 2p spectra, (d) high-resolution C 1s spectra, (e) high-resolution N 1s spectra, (f) high-resolution O 1s spectra of the resultant $\text{Co(OH)}_2@\text{ZIF-67}$ and $\text{B-Co}_3\text{O}_4\text{-1}@\text{ZIF-67}$; (c) high-resolution B 1s spectra of the resultant $\text{B-Co}_3\text{O}_4\text{-1}@\text{ZIF-67}$, Figure S14: EPR spectra of the resultant $\text{B-Co}_3\text{O}_4\text{-1}@\text{ZIF-67}$ and $\text{B-Co}_3\text{O}_4\text{-2}@\text{ZIF-67}$, Figure S15: Electrochemical performances of the resultant $\text{B-Co}_3\text{O}_4\text{-1}$, $\text{B-Co}_3\text{O}_4\text{-2}$, and $\text{B-Co}_3\text{O}_4\text{-2}@\text{ZIF-67}$ in 1.0 M KOH: (a) polarization curves with iR compensation, (b) Tafel slope plots, (c) current density as a function of scan rate derived from the CV curves at different scan rates and (d) Nyquist plots, Figure S16: Electrochemical performances of the resultant ZIF-67, $\text{Co(OH)}_2@\text{ZIF-67}$, and $\text{B-Co}_3\text{O}_4\text{-2}@\text{ZIF-67}$ in 1.0 M KOH: (a) polarization curves with iR compensation, (b) Tafel slope plots, and (c) Nyquist plots, Figure S17: (a,c,e) CV curves at different scan rates (5, 10, 15, 20 and 25 mV s^{-1}) and (b,d,f) current density as a function of scan rate derived from the CV curves at different scan rates for the resultant $\text{B-Co}_3\text{O}_4\text{-1}@\text{ZIF-67}$ (a,b), $\text{B-Co}_3\text{O}_4\text{-2}@\text{ZIF-67}$ (c,d), and $\text{CoBi}/\text{ZIF-67}$ (e,f) in 1.0 M KOH, Figure S18: (a,c,e,g) CV curves at different scan rates (5, 10, 15, 20 and 25 mV s^{-1}) and (b,d,f,h) current density as a function of scan rate derived from the CV curves at different scan rates for the resultant $\text{B-Co}_3\text{O}_4\text{-1}$ (a,b), $\text{B-Co}_3\text{O}_4\text{-2}$ (c,d), Co(OH)_2 (e,f) and ZIF-

67 (g,h) in 1.0 M KOH solution, Figure S19: Low-magnification (a) and high-magnification (b) FESEM images of the resultant B-Co₃O₄-2@ZIF-67 after OER durability test, Figure S20: High-resolution XPS Co 2p spectra (a), B 1s spectra (b), C 1s spectra (c), O 1s spectra (d) of the resultant B-Co₃O₄-2@ZIF-67 before and after the stability test, Table S1: Summary of nitrogen adsorption-desorption isotherm data of the resultant B-Co₃O₄-1@ZIF-67 and B-Co₃O₄-2@ZIF-67, Table S2: The EDX results of the resultant B-Co₃O₄-1 and B-Co₃O₄-2. (The element content is atomic percentage), Table S3: The XPS element atomic content percentage and Co³⁺/Co²⁺ ratio of the test samples, Table S4: Summary of the electrochemical data of all the samples for OER in 1.0 M KOH solution, Table S5: The EDX results of the B-Co₃O₄-2@ZIF-67 catalyst before and after OER test. (The element content is atomic percentage), Table S6: Comparison of OER catalytic activity between B-Co₃O₄-2@ZIF-67 sample and other electrocatalysts in alkaline solution.

Author Contributions: Designed and performed the experiments, X.L.; analyzed the experimental data, X.L. aided in data collection, H.L.; data interpretation and plotting, H.L.; contributed to Tafel slope and EIS analysis, G.H.; contributed to the preparation of ZIF-67 precursor, Y.Z.; contributed to literature search and edited the manuscript, J.X.; wrote the manuscript, X.L.; supervised the project, revised and edited the manuscript, L.H. All authors have read and agreed to the published version of the manuscript.

Funding: This research was funded by the Fundamental Research Funds for the Central Universities (Project No.531118010232) and the Huxiang High-Level Talent Gathering Project of Hunan Province (Project No.2019RS1012).

Institutional Review Board Statement: Not application.

Informed Consent Statement: Not application.

Data Availability Statement: The data presented in this study are available on request from the corresponding author.

Conflicts of Interest: The authors declare no conflict of interest.

References

1. Yang, D.; Su, Z.; Chen, Y.; Srinivas, K.; Gao, J.; Zhang, W.; Wang, Z.; Lin, H. Electronic modulation of hierarchical spongy nanosheets toward efficient and stable water electrolysis. *Small* **2021**, *17*, 2006881. [[CrossRef](#)] [[PubMed](#)]
2. Zhang, Z.; Zhang, T.; Lee, J.Y. 110th Anniversary: A total water splitting electrocatalyst based on borate/Fe Co-doping of nickel sulfide. *Ind. Eng. Chem. Res.* **2019**, *58*, 13053–13063. [[CrossRef](#)]
3. Zang, W.; Sun, T.; Yang, T.; Xi, S.; Waqar, M.; Kou, Z.; Lyu, Z.; Feng, Y.P.; Wang, J.; Pennycook, S.J. Efficient hydrogen evolution of oxidized Ni-N₃ defective sites for alkaline freshwater and seawater electrolysis. *Adv. Mater.* **2021**, *33*, 2003846. [[CrossRef](#)]
4. Yu, J.; Wang, J.; Long, X.; Chen, L.; Cao, Q.; Wang, J.; Qiu, C.; Lim, J.; Yang, S. Formation of FeOOH nanosheets induces substitutional doping of CeO_{2-x} with high-valence Ni for efficient water oxidation. *Adv. Energy Mater.* **2020**, *11*, 2002731. [[CrossRef](#)]
5. Zhu, J.; Wei, M.; Meng, Q.; Chen, Z.; Fan, Y.; Hasan, S.W.; Zhang, X.; Lyu, D.; Tian, Z.Q.; Shen, P.K. Ultrathin-shell IrCo hollow nanospheres as highly efficient electrocatalysts towards the oxygen evolution reaction in acidic media. *Nanoscale* **2020**, *12*, 24070–24078. [[CrossRef](#)]
6. Quang, N.D.; Majumder, S.; Van, P.C.; Jeong, J.-R.; Kim, C.; Kim, D. Co₃O₄/reduced graphene oxide/BiVO₄ nanorod as high performance photoanode for water oxidation. *Electrochim. Acta* **2020**, *364*, 137283–137293. [[CrossRef](#)]
7. Lei, Y.; Xu, T.; Ye, S.; Zheng, L.; Liao, P.; Xiong, W.; Hu, J.; Wang, Y.; Wang, J.; Ren, X.; et al. Engineering defect-rich Fe-doped NiO coupled Ni cluster nanotube arrays with excellent oxygen evolution activity. *Appl. Catal. B Environ.* **2021**, *285*, 119809–119818. [[CrossRef](#)]
8. Zhang, S.L.; Guan, B.Y.; Lu, X.F.; Xi, S.; Du, Y.; Lou, X.W.D. Metal atom-doped Co₃O₄ hierarchical nanoplates for electrocatalytic oxygen evolution. *Adv. Mater.* **2020**, *32*, 2002235. [[CrossRef](#)]
9. Dong, F.; Li, L.; Kong, Z.; Xu, X.; Zhang, Y.; Gao, Z.; Dongyang, B.; Ni, M.; Liu, Q.; Lin, Z. Materials engineering in perovskite for optimized oxygen evolution electrocatalysis in alkaline condition. *Small* **2021**, *17*, 2006638. [[CrossRef](#)] [[PubMed](#)]
10. Huang, Y.; Wei, G.; He, J.; An, C.; Hu, M.; Shu, M.; Zhu, J.; Yao, S.; Xi, W.; Si, R.; et al. Interfacial electronic interaction of atomically dispersed IrCl_x on ultrathin Co(OH)₂/CNTs for efficient electrocatalytic water oxidation. *Appl. Catal. B Environ.* **2020**, *279*, 119398–119405. [[CrossRef](#)]
11. Srinivas, K.; Chen, Y.; Wang, B.; Yu, B.; Lu, Y.; Su, Z.; Zhang, W.; Yang, D. Metal-organic framework-derived Fe-doped Ni₃Fe/NiFe₂O₄ heteronanoparticle-decorated carbon nanotube network as a highly efficient and durable bifunctional electrocatalyst. *ACS Appl. Mater. Interfaces* **2020**, *12*, 55782–55794. [[CrossRef](#)]

12. Moschkowitsch, W.; Dhaka, K.; Gonen, S.; Attias, R.; Tsur, Y.; Caspary Toroker, M.; Elbaz, L. Ternary NiFeTiOOH catalyst for the oxygen evolution reaction: Study of the effect of the addition of Ti at different loadings. *ACS Catal.* **2020**, *10*, 4879–4887. [[CrossRef](#)]
13. Choi, J.; Kim, D.; Zheng, W.; Yan, B.; Li, Y.; Lee, L.Y.S.; Piao, Y. Interface engineered NiFe₂O_{4-x}/NiMoO₄ nanowire arrays for electrochemical oxygen evolution. *Appl. Catal. B Environ.* **2021**, *286*, 119857–119865. [[CrossRef](#)]
14. Liu, Z.; Yu, X.; Xue, H.; Feng, L. A nitrogen-doped CoP nanoarray over 3D porous Co foam as an efficient bifunctional electrocatalyst for overall water splitting. *J. Mater. Chem. A* **2019**, *7*, 13242–13248. [[CrossRef](#)]
15. Yuan, G.; Bai, J.; Zhang, L.; Chen, X.; Ren, L. The effect of P vacancies on the activity of cobalt phosphide nanorods as oxygen evolution electrocatalyst in alkali. *Appl. Catal. B Environ.* **2021**, *284*, 119693–119701. [[CrossRef](#)]
16. Naderi, A.; Yong, X.; Karamad, M.; Cai, J.; Zang, Y.; Gates, I.; Siahrostami, S.; Wang, G. Ternary cobalt–iron sulfide as a robust electrocatalyst for water oxidation: A dual effect from surface evolution and metal doping. *Appl. Sur. Sci.* **2021**, *542*, 148681–148687. [[CrossRef](#)]
17. Masa, J.; Weide, P.; Peeters, D.; Sinev, I.; Xia, W.; Sun, Z.; Somsen, C.; Muhler, M.; Schuhmann, W. Amorphous cobalt boride (Co₂B) as a highly efficient nonprecious catalyst for electrochemical water splitting: Oxygen and hydrogen evolution. *Adv. Energy Mater.* **2016**, *6*, 1502313. [[CrossRef](#)]
18. Yi, L.; Niu, Y.; Feng, B.; Zhao, M.; Hu, W. Simultaneous phase transformation and doping via a unique photochemical–electrochemical strategy to achieve a highly active Fe-doped Ni oxyhydroxide oxygen evolution catalyst. *J. Mater. Chem. A* **2021**, *9*, 4213–4220. [[CrossRef](#)]
19. Xu, Z.; Ying, Y.; Zhang, G.; Li, K.; Liu, Y.; Fu, N.; Guo, X.; Yu, F.; Huang, H. Engineering NiFe layered double hydroxide by valence control and intermediate stabilization toward the oxygen evolution reaction. *J. Mater. Chem. A* **2020**, *8*, 26130–26138. [[CrossRef](#)]
20. He, J.; Zhou, X.; Xu, P.; Sun, J. Promoting electrocatalytic water oxidation through tungsten–modulated oxygen vacancies on hierarchical FeNi-layered double hydroxide. *Nano Energy* **2021**, *80*, 105540–105548. [[CrossRef](#)]
21. Xu, L.; Wang, Z.; Wang, J.; Xiao, Z.; Huang, X.; Liu, Z.; Wang, S. N-doped nanoporous Co₃O₄ nanosheets with oxygen vacancies as oxygen evolving electrocatalysts. *Nanotechnology* **2017**, *28*, 165402–165409. [[CrossRef](#)]
22. Zhang, J.; Qian, J.; Ran, J.; Xi, P.; Yang, L.; Gao, D. Engineering lower coordination atoms onto NiO/Co₃O₄ heterointerfaces for boosting oxygen evolution reactions. *ACS Catal.* **2020**, *10*, 12376–12384. [[CrossRef](#)]
23. Zeng, H.; Oubla, M.H.; Zhong, X.; Alonso-Vante, N.; Du, F.; Xie, Y.; Huang, Y.; Ma, J. Rational defect and anion chemistries in Co₃O₄ for enhanced oxygen evolution reaction. *Appl. Catal. B Environ.* **2021**, *281*, 119535–119543. [[CrossRef](#)]
24. Zou, L.; Xu, Q. Synthesis of a hierarchically porous C/Co₃O₄ nanostructure with boron doping for oxygen evolution reaction. *Chem. Asian J.* **2020**, *15*, 490–493. [[CrossRef](#)] [[PubMed](#)]
25. Xia, H.; Huang, Z.; Lv, C.; Zhang, C. A self-supported porous hierarchical core–shell nanostructure of cobalt oxide for efficient oxygen evolution reaction. *ACS Catal.* **2017**, *7*, 8205–8213. [[CrossRef](#)]
26. Zhang, B.; Jiang, K.; Wang, H.; Hu, S. Fluoride-induced dynamic surface self-reconstruction produces unexpectedly efficient oxygen-evolution catalyst. *Nano Lett.* **2019**, *19*, 530–537. [[CrossRef](#)]
27. Wang, Q.; Xue, X.; Lei, Y.; Wang, Y.; Feng, Y.; Xiong, X.; Wang, D.; Li, Y. Engineering of electronic states on Co₃O₄ ultrathin nanosheets by cation substitution and anion vacancies for oxygen evolution reaction. *Small* **2020**, *16*, 2001571. [[CrossRef](#)] [[PubMed](#)]
28. Chen, C.; Yang, Z.; Liang, W.; Yan, H.; Tuo, Y.; Li, Y.; Zhou, Y.; Zhang, J. Ultra-small Co/CoO nanoparticles dispersed on N-doped carbon nanosheets for highly efficient electrocatalytic oxygen evolution reaction. *J. Energy Chem.* **2021**, *55*, 345–354. [[CrossRef](#)]
29. Liu, T.; Zhang, L.; You, W.; Yu, J. Core-shell nitrogen-doped carbon hollow spheres/Co₃O₄ nanosheets as advanced electrode for high-performance supercapacitor. *Small* **2018**, *14*, 1702407–1702414. [[CrossRef](#)] [[PubMed](#)]
30. Li, H.; Tan, M.; Huang, C.; Luo, W.; Yin, S.-F.; Yang, W. Co₂(OH)₃Cl and MOF mediated synthesis of porous Co₃O₄/NC nanosheets for efficient OER catalysis. *Appl. Sur. Sci.* **2021**, *542*, 148739–148747. [[CrossRef](#)]
31. Yuan, H.; Wang, S.; Ma, Z.; Kundu, M.; Tang, B.; Li, J.; Wang, X. Oxygen vacancies engineered self-supported B doped Co₃O₄ nanowires as an efficient multifunctional catalyst for electrochemical water splitting and hydrolysis of sodium borohydride. *Chem. Eng. J.* **2021**, *404*, 126474–126486. [[CrossRef](#)]
32. Wang, Z.; Xu, W.; Chen, X.; Peng, Y.; Song, Y.; Lv, C.; Liu, H.; Sun, J.; Yuan, D.; Li, X.; et al. Defect-rich nitrogen doped Co₃O₄/C porous nanocubes enable high-efficiency bifunctional oxygen electrocatalysis. *Adv. Funct. Mater.* **2019**, *29*, 1902875. [[CrossRef](#)]
33. Yang, H.; Chen, Z.; Guo, P.; Fei, B.; Wu, R. B-doping-induced amorphization of LDH for large-current-density hydrogen evolution reaction. *Appl. Catal. B Environ.* **2020**, *261*, 118240–118248. [[CrossRef](#)]
34. Lai, Y.; Xiao, L.; Tao, Y.; Gao, Z.; Zhang, L.; Su, X.; Dai, Y. Enhancing one-dimensional charge transport in metal-organic framework hexagonal nanorods for electrocatalytic oxygen evolution. *ChemSusChem* **2021**, *14*, 1–6. [[CrossRef](#)] [[PubMed](#)]
35. Lin, Y.; Zhang, M.; Zhao, L.; Wang, L.; Cao, D.; Gong, Y. Ru doped bimetallic phosphide derived from 2D metal organic framework as active and robust electrocatalyst for water splitting. *Appl. Sur. Sci.* **2021**, *536*, 147952–147964. [[CrossRef](#)]
36. Weng, Y.G.; Yin, W.Y.; Jiang, M.; Hou, J.L.; Shao, J.; Zhu, Q.Y.; Dai, J. Tetrathiafulvalene-based metal-organic framework as a high-performance anode for lithium-ion batteries. *ACS Appl. Mater. Interfaces* **2020**, *12*, 52615–52623. [[CrossRef](#)] [[PubMed](#)]
37. Cheng, N.; Wang, N.; Ren, L.; Casillas-Garcia, G.; Liu, N.; Liu, Y.; Xu, X.; Hao, W.; Dou, S.X.; Du, Y. In-situ grafting of N-doped carbon nanotubes with Ni encapsulation onto MOF-derived hierarchical hybrids for efficient electrocatalytic hydrogen evolution. *Carbon* **2020**, *163*, 178–185. [[CrossRef](#)]

38. Marks, S.D.; Riascos-Rodriguez, K.; Arrieta-Pérez, R.R.; Yakovenko, A.A.; Exley, J.; Evans, P.G.; Hernández-Maldonado, A.J. Lattice expansion and ligand twist during CO₂ adsorption in flexible Cu bipyridine metal–organic frameworks. *J. Mater. Chem. A* **2020**, *8*, 18903–18915. [[CrossRef](#)]
39. Mohan, M.; Essalhi, M.; Durette, D.; Rana, L.K.; Ayevide, F.K.; Maris, T.; Duong, A. A rational design of microporous nitrogen-rich lanthanide metal-organic frameworks for CO₂/CH₄ separation. *ACS Appl. Mater. Interfaces* **2020**, *12*, 50619–50627. [[CrossRef](#)]
40. Zhu, J.; Liu, C.; Sun, J.; Xing, Y.; Quan, B.; Li, D.; Jiang, D. Interfacial engineering of Co₃FeN embedded N-doped carbon nanoarray derived from metal–organic frameworks for enhanced oxygen evolution reaction. *Electrochim. Acta* **2020**, *354*, 136629–136636. [[CrossRef](#)]
41. Wang, C.; Chen, W.; Yuan, D.; Qian, S.; Cai, D.; Jiang, J.; Zhang, S. Tailoring the nanostructure and electronic configuration of metal phosphides for efficient electrocatalytic oxygen evolution reactions. *Nano Energy* **2020**, *69*, 104453–104460. [[CrossRef](#)]
42. Wu, H.B.; Guan, B.Y.; He, P.; Yu, X.-Y. Synthesis of ZIF-67 nanocubes with complex structures co-mediated by dopamine and polyoxometalate. *J. Mater. Chem. A* **2018**, *6*, 19338–19341. [[CrossRef](#)]
43. Lv, Z.; Zhong, Q.; Bu, Y. Controllable synthesis of Ni-Co nanosheets covered hollow box via altering the concentration of nitrate for high performance supercapacitor. *Electrochim. Acta* **2016**, *215*, 500–505. [[CrossRef](#)]
44. Chen, W.; Han, B.; Tian, C.; Liu, X.; Liang, S.; Deng, H.; Lin, Z. MOFs-derived ultrathin holey Co₃O₄ nanosheets for enhanced visible light CO₂ reduction. *Appl. Catal. B Environ.* **2019**, *244*, 996–1003. [[CrossRef](#)]
45. Silva, F.L.G.; Veiga, A.G.; Carvalho, N.M.F. Manganese oxides treated with organic compounds as catalysts for water oxidation reaction. *Int. J. Hydrog. Energy* **2021**, *46*, 11677–11687. [[CrossRef](#)]
46. Wang, H.; Fu, W.; Chen, Y.; Xue, F.; Shan, G. ZIF-67-derived Co₃O₄ hollow nanocage with efficient peroxidase mimicking characteristic for sensitive colorimetric biosensing of dopamine. *Spectrochim. Acta A Mol. Biomol. Spectrosc.* **2021**, *246*, 119006–119015. [[CrossRef](#)]
47. Garg, N.; Kumar, M.; Kumari, N.; Deep, A.; Sharma, A.L. Chemoresistive room-temperature sensing of ammonia using zeolite imidazole framework and reduced graphene oxide (ZIF-67/rGO) composite. *ACS Omega* **2020**, *5*, 27492–27501. [[CrossRef](#)]
48. Pei, W.; Zhang, J.; Tong, H.; Ding, M.; Shi, F.; Wang, R.; Huo, Y.; Li, H. Removal and reutilization of metal ions on ZIF-67/GO membrane via synergistic photocatalytic-photothermal route. *Appl. Catal. B Environ.* **2021**, *282*, 119575–119584. [[CrossRef](#)]
49. Jafarinasab, M.; Akbari, A.; Omidkhah, M.; Shakeri, M. An efficient Co-based metal–organic framework nanocrystal (Co-ZIF-67) for adsorptive desulfurization of dibenzothiophene: Impact of the preparation approach on structure tuning. *Energy Fuels* **2020**, *34*, 12779–12791. [[CrossRef](#)]
50. Chameh, B.; Moradi, M.; Hajati, S.; Hessari, F.A. Design and construction of ZIF(8 and 67) supported Fe₃O₄ composite as advanced materials of high performance supercapacitor. *Phys. E Low Dimens. Syst. Nanostruct.* **2021**, *126*, 114442–114452. [[CrossRef](#)]
51. Modi, A.; Bellare, J. Zeolitic imidazolate framework-67/carboxylated graphene oxide nanosheets incorporated polyethersulfone hollow fiber membranes for removal of toxic heavy metals from contaminated water. *Sep. Purif. Technol.* **2020**, *249*, 117160–117169. [[CrossRef](#)]
52. Qin, J.; Wang, S.; Wang, X. Visible-light reduction CO₂ with dodecahedral zeolitic imidazolate framework ZIF-67 as an efficient co-catalyst. *Appl. Catal. B Environ.* **2017**, *209*, 476–482. [[CrossRef](#)]
53. Xu, W.; Wang, X.; Wu, Y.; Li, W.; Chen, C. Functionalized graphene with Co-ZIF adsorbed borate ions as an effective flame retardant and smoke suppression agent for epoxy resin. *J. Hazard Mater.* **2019**, *363*, 138–151. [[CrossRef](#)] [[PubMed](#)]
54. Cheng, K.; Cao, D.; Yang, F.; Xu, Y.; Sun, G.; Ye, K.; Yin, J.; Wang, G. Facile synthesis of morphology-controlled Co₃O₄ nanostructures through solvothermal method with enhanced catalytic activity for H₂O₂ electroreduction. *J. Power Sources* **2014**, *253*, 214–223. [[CrossRef](#)]
55. Zhou, T.; Lu, P.; Zhang, Z.; Wang, Q.; Umar, A. Perforated Co₃O₄ nanoneedles assembled in chrysanthemum-like Co₃O₄ structures for ultra-high sensitive hydrazine chemical sensor. *Sens. Actuators B Chem.* **2016**, *235*, 457–465. [[CrossRef](#)]
56. Zhang, R.; Ke, W.; Chen, S.; Yue, X.; Hu, Z.; Ning, T. Phase evolution of vulcanized Co₃O₄ catalysts during oxygen evolution reaction. *Appl. Sur. Sci.* **2021**, *546*, 148819. [[CrossRef](#)]
57. Yan, W.; Shen, Y.; An, C.; Li, L.; Si, R.; An, C. FeO_x clusters decorated hcp Ni nanosheets as inverse electrocatalyst to stimulate excellent oxygen evolution performance. *Appl. Catal. B Environ.* **2021**, *284*, 119687–119695. [[CrossRef](#)]
58. Zhang, J.; Zhao, Z.; Xia, Z.; Dai, L. A metal-free bifunctional electrocatalyst for oxygen reduction and oxygen evolution reactions. *Nat. Nanotechnol.* **2015**, *10*, 444–452. [[CrossRef](#)]
59. Guo, M.; Qu, Y.; Yuan, C.; Chen, S. Electrochemical exfoliation of hierarchical Co₃O₄ microflowers and their conversion into CoP as high-efficiency hydrogen evolution electrocatalyst. *Electrochim. Acta* **2019**, *322*, 134768–134777. [[CrossRef](#)]
60. Vikraman, D.; Hussain, S.; Karuppasamy, K.; Feroze, A.; Kathalingam, A.; Sanmugam, A.; Chun, S.-H.; Jung, J.; Kim, H.-S. Engineering the novel MoSe₂-Mo₂C hybrid nanoarray electrodes for energy storage and water splitting applications. *Appl. Catal. B Environ.* **2020**, *264*, 118531–118543. [[CrossRef](#)]
61. Li, Y.; Li, F.-M.; Meng, X.-Y.; Li, S.-N.; Zeng, J.-H.; Chen, Y. Ultrathin Co₃O₄ nanomeshes for the oxygen evolution reaction. *ACS Catal.* **2018**, *8*, 1913–1920. [[CrossRef](#)]
62. Zhang, Z.; Zhang, T.; Lee, J.Y. Enhancement effect of borate doping on the oxygen evolution activity of α-nickel hydroxide. *ACS Appl. Nano Mater.* **2018**, *1*, 751–758. [[CrossRef](#)]

63. Wang, X.; Zhou, L.; Yang, T.; Gao, J.; He, P.; Jia, L.; Dong, F.; Jia, B.; Zhang, H. Facile one-step synthesis of tunable nanochain-like Fe–Mo–B: A highly efficient and stable catalyst for oxygen evolution reaction. *J. Alloys Compd.* **2020**, *822*, 153517–153524. [[CrossRef](#)]
64. Yang, Y.X.; Li, B.L.; Zhang, Q.; Guo, W.H.; Wang, X.H.; Li, L.J.; Luo, H.Q.; Li, N.B. Prussian blue analogues-derived CoFe–B nanocubes with increased specific surface area and modulated electronic structure as enhanced oxygen evolution electrocatalysts. *Energy Technol.* **2020**, *9*, 2000178. [[CrossRef](#)]
65. Xiao, Z.; Wang, Y.; Huang, Y.-C.; Wei, Z.; Dong, C.-L.; Ma, J.; Shen, S.; Li, Y.; Wang, S. Filling the oxygen vacancies in Co₃O₄ with phosphorus: An ultra-efficient electrocatalyst for overall water splitting. *Energy Environ. Sci.* **2017**, *10*, 2563–2569. [[CrossRef](#)]
66. Ji, L.; Wang, J.; Teng, X.; Meyer, T.J.; Chen, Z. CoP nanoframes as bifunctional electrocatalysts for efficient overall water splitting. *ACS Catal.* **2019**, *10*, 412–419. [[CrossRef](#)]
67. Yang, X.; Chen, J.; Chen, Y.; Feng, P.; Lai, H.; Li, J.; Luo, X. Novel Co₃O₄ nanoparticles/nitrogen-doped carbon composites with extraordinary catalytic activity for oxygen evolution reaction (OER). *Nano-Micro Lett.* **2018**, *10*, 15–25. [[CrossRef](#)] [[PubMed](#)]
68. Lian, Y.; Sun, H.; Wang, X.; Qi, P.; Mu, Q.; Chen, Y.; Ye, J.; Zhao, X.; Deng, Z.; Peng, Y. Carved nanoframes of cobalt-iron bimetal phosphide as a bifunctional electrocatalyst for efficient overall water splitting. *Chem. Sci.* **2019**, *10*, 464–474. [[CrossRef](#)]
69. Liu, P.F.; Yang, S.; Zhang, B.; Yang, H.G. Defect-rich ultrathin cobalt-iron layered double hydroxide for electrochemical overall water splitting. *ACS Appl. Mater. Interfaces* **2016**, *8*, 34474–34481. [[CrossRef](#)] [[PubMed](#)]
70. Zhuang, L.; Ge, L.; Yang, Y.; Li, M.; Jia, Y.; Yao, X.; Zhu, Z. Ultrathin iron-cobalt oxide nanosheets with abundant oxygen vacancies for the oxygen evolution reaction. *Adv. Mater.* **2017**, *29*, 1606793–1606799. [[CrossRef](#)] [[PubMed](#)]
71. Xie, M.; Ma, Y.; Lin, D.; Xu, C.; Xie, F.; Zeng, W. Bimetal-organic framework MIL-53(Co-Fe): An efficient and robust electrocatalyst for the oxygen evolution reaction. *Nanoscale* **2020**, *12*, 67–71. [[CrossRef](#)] [[PubMed](#)]
72. Liu, S.; Zhang, J.; Wang, H.; Asefa, T.; Huang, X. A facile route to efficient water oxidation electrodes via electrochemical activation of iron in nickel sulfate solution. *ACS Sustain. Chem. Eng.* **2020**, *8*, 15550–15559. [[CrossRef](#)]
73. Qu, M.; Jiang, Y.; Yang, M.; Liu, S.; Guo, Q.; Shen, W.; Li, M.; He, R. Regulating electron density of NiFe-P nanosheets electrocatalysts by a trifle of Ru for high-efficient overall water splitting. *Appl. Catal. B Environ.* **2020**, *263*, 118324–118332. [[CrossRef](#)]
74. Wang, T.; Zhang, X.; Zhu, X.; Liu, Q.; Lu, S.; Asiri, A.M.; Luo, Y.; Sun, X. Hierarchical CuO@ZnCo LDH heterostructured nanowire arrays toward enhanced water oxidation electrocatalysis. *Nanoscale* **2020**, *12*, 5359–5362. [[CrossRef](#)] [[PubMed](#)]
75. Hoang, V.C.; Dinh, K.N.; Gomes, V.G. Hybrid Ni/NiO composite with N-doped activated carbon from waste cauliflower leaves: A sustainable bifunctional electrocatalyst for efficient water splitting. *Carbon* **2020**, *157*, 515–524. [[CrossRef](#)]